2016

Impact of scale/resolution on evapotranspiration from Landsat and MODIS images

Vivek Sharma
University of Nebraska-Lincoln, vivekpathankot@gmail.com

Ayse Kilic
University of Nebraska-Lincoln, akilic@unl.edu

Suat Irmak
University of Nebraska-Lincoln, suat.irmak@unl.edu

AGU PUBLICATIONS

Water Resources Research

RESEARCH ARTICLE
10.1002/2015WR017772

Key Points:
- The effects of pixel scales on ETc was determined
- Spatially distributed ETc values were estimated from Landsat and MODIS
- Output flux aggregation and input up-scaling procedure were conducted

Correspondence to:
S. Irmak,
sirmak2@unl.edu

Citation:
Sharma, V., A. Kilic, and S. Irmak (2016), Impact of scale/resolution on evapotranspiration from Landsat and MODIS images, *Water Resour. Res.*, *52*, 1800–1819, doi:10.1002/2015WR017772.

Received 30 JUN 2015
Accepted 15 FEB 2016
Accepted article online 17 FEB 2016
Published online 11 MAR 2016

Impact of scale/resolution on evapotranspiration from Landsat and MODIS images

Vivek Sharma[1], Ayse Kilic[2], and Suat Irmak[1]

[1]Department of Biological Systems Engineering, University of Nebraska-Lincoln, Lincoln, Nebraska, USA, [2]Department of Civil Engineering, School of Natural Resources, University of Nebraska-Lincoln, Lincoln, Nebraska, USA

Abstract Understanding the role of landscape heterogeneity and its influence on the scaling behavior of surface fluxes as observed by satellite sensors with different spatial resolutions is a critical need to investigate. In this study, the effects of pixel scales on *ETc* estimation and other parameters that are used to calculate *ETc* were investigated over different vegetation surfaces in south central Nebraska, USA. Surface Energy Balance System (SEBS) was used to estimate spatially distributed *ETc* by combining ground-based meteorological data for Landsat and MODIS imagery. The estimated surface energy fluxes were compared and validated to the measured Bowen Ratio Energy Balance System (BREBS) *ETc* fluxes. Validation results showed that Landsat has more preferable spatial resolution (30 m) to map and analyze *ETc*; regression models explained 91% of the variability in the observed data (RMSD = 0.064 mm/h; MBE = 0.04 mm/h). However, for MODIS-based *ETc*, the regression model explained only 59% of the variability in observed ETc with a larger error (RMSD = 0.17 mm/h; MBE = 0.15 mm/h). MODIS-based *ETc* was about 31% higher than the measured *ETc*. Imperfect assessment in MODIS-based retrievals is due to the underlying assumption of spatial heterogeneity and coarser sensor pixel scale (500 m), which was summarized by up-scaling the Landsat images to MODIS images using output flux aggregation and input up-scaling procedure using simple average and nearest neighbor aggregation techniques and comparisons were made on both image and pixel scales. Aggregation results illustrate that simple average with output flux aggregation provides close interpretation in aggregating fluxes to coarser resolution than other aggregation approaches. Pixel-by-pixel comparison using output aggregation with simple average resulted in close agreement (error range 5%–35%) between measured and up-scaled fluxes, compared to input up-scaling using simple average (error range 25%–60%). Larger error in input up-scaling is due to the changes in the surface roughness parameters due to aggregation in SEBS model. In addition, the magnitude of errors in *ETc* estimation was observed to be a function of the heterogeneity of the land surface and evaporative elements over the study region. Comparison between up-scaled *ETc* at 480 m spatial resolution with original MODIS image at 500 m showed that the output aggregation using simple average aggregation method provided closer representation of *ETc* at 500 m MODIS pixel resolution than the nearest neighbor resampling method.

1. Introduction

One of the important questions related to scaling-up of surface energy balance variables in agro-ecosystems is "how scaling and resolution potentially affect the distribution of fluxes over the land surface?" [*Gibson et al.*, 2000]. Representing the variation in various land use/land cover, soil, and atmospheric parameters at larger scale is difficult due to the challenges of spatial heterogeneity of the land surface. Various models have been developed to monitor land-atmosphere energy balance flux interactions, where spatially variable inputs and parameters are based on assumptions, in most cases, of the homogeneity of the land and atmospheric surfaces and widely used in many large-scale hydrologic and water balance studies. However, the outcome of these models mostly ignores many of the small-scale interactions, smaller than the grid cell in the model [*Sridhar et al.*, 2003]. In reality, the assumption of homogeneity is rarely met. Therefore, necessary analysis in terms of the effect of scale in predicting the energy balances fluxes at multiple scales should be conducted to understand the physical mechanisms for various climatic, weather, and surface energy balance modeling.

Crop evapotranspiration (*ETc*) is one of the most critical components of the hydrological cycle, which is very complex and highly variable process both in space and time, especially on large scales over heterogeneous surfaces. *ETc* is influenced by surface characteristics, including soil water status and vegetation height; environmental parameters such as land surface temperature, air temperature, relative humidity (vapor pressure deficit), incoming shortwave radiation, and wind speed; and other factors. Consequently, reliable accounting/balance of the water resources, availability, and distribution of earth's water and response of vegetation to changes in climate and water resources depends on the accurate estimation of *ETc*. While there are spatially discrete and highly accurate techniques available to estimate these surface energy balance fluxes, including *ETc* at point/field scales (e.g., Bowen Ratio Energy Balance System, lysimeters, eddy covariance system, scintillometers, and surface renewal) and that they provide invaluable/critical data for calibration and validation of remote sensing/satellite-based estimates, these ground-based fluxes, in some cases, need to be scaled-up to larger scales. Satellite/remote sensing methods coupled with geographically information system (GIS) tools enable developing, extrapolating, and mapping of the fluxes to larger scales that can aid in watershed or regional water balance analyses. The multiband satellite sensors can provide vegetation and thermal information at different spatial, temporal, spectral, and radiometric resolution and is closely related to energy and heat transfer processes. Several satellite/remote sensing-based empirical relationships have been developed to determine *ETc* and other energy balance fluxes including the Surface Energy Balance Index (SEBI) [*Menenti and Choudhary*, 1993], Simplified Surface Energy Balance Index (S-SEBI) [*Roerink et al*., 2000], Surface Energy Balance System (SEBS) [*Su*, 2002], Surface Energy Balance Algorithm for Land (SEBAL) [*Bastiaanssen et al*., 1998], Mapping Evapotranspiration at High Resolution with Internalized Calibration (METRIC) [*Allen et al*., 2007], and others. These models have been applied at local and regional scales to estimate surface energy fluxes in combination with field and/or metrological observations. Determining the flux data from these models with individual satellite platforms has been addressed in many studies [*Sharma et al*., 2015; *Ma et al*., 2012; *Jia et al*., 2009; *Jiang et al*., 2009]; however, the intercomparison between sensors and subsequent effect of spatial resolution on flux determination is addressed in few studies [*Hong et al*., 2009; *McCabe and Wood*, 2006; *Kustas et al*., 2004].

To address the issues of spatial resolution of pixels on energy fluxes, first the consistency of energy balance flux estimation from different satellite sensors needs to be considered. For example, spatial resolution of remotely sensed *ETc* and other energy balance fluxes depends on the specification of satellite sensors, which further depends primarily on the scale of the study area to be analyzed. For large study area, it is difficult to obtain high-resolution imagery on a continuous basis, but in many cases, the high-resolution products are not easily available due to low temporal variability, cloud cover, and high costs. On the other hand, low-resolution remote sensing data such as Advanced Very High Resolution Radiometer (AVHRR) and Moderate Resolution Imaging Spectroradiometer (MODIS) product cannot consider the heterogeneity of land surface characteristics, which may result in potential error in flux estimation. Spatial resolution/scaling is also considered as the important component in the validation of remote sensing algorithms [*Ershadi et al*., 2013; *Hong et al*., 2009; *Liang*, 2005; *Brunsell and Gillies*, 2003; *Sridhar et al*., 2003; *Su et al*., 1999]. Major limitations to this approach may include the issue of scaling of the satellite measurements, i.e., comparison of measurements at varying scales. For example, point/field measurement can and should be used to validate the fine-resolution products such as Landsat (spatial resolution = 30 m), but such measurements may not be directly applicable to validate the high-resolution product from MODIS (spatial resolution = 250, 500, and 1000 m), AVHRR, etc. (spatial resolution = 1000 m), due to scale discrepancy between point measurement and coarse spatial resolution. Therefore, to validate the coarser resolution data, the Landsat product was scaled-up and this can be done by using different aggregation methods.

Aggregation of remotely sensed variables becomes more complicated when dealing with the heterogeneity of the land surface [*Famiglietti and Wood*, 1994; *Giorgi*, 1997; *Su et al*., 1999; *Brunsell and Gillies*, 2003; *Sridhar et al*., 2003; *Brunsell*, 2011] because of the nonlinearity in surface energy balance fluxes at the land-atmosphere interface. During the aggregation process, the original spatial data are reduced to a smaller number of data units (less number of pixels) [*Bian and Butler*, 1999]. As a result, each aggregated data unit represents the larger pixel than the original image. Some studies reported the up-scaling process of data [*Nellis and Briggs*, 1989; *Lam and Quattrochi*, 1992; *Vieux*, 1993; *Zhang and Montgomery*, 1994; *Bian and Butler*, 1999]. *Moran et al*. [1997] evaluated the effect of radiance aggregation on temperature and sensible heat over semiarid rangeland of Arizona and observed large errors as over 50% in the sensible heat

estimates, and they indicated that the large errors are mainly due to variation (nonlinearity) in atmospheric stability and aerodynamic roughness over heterogeneous land surfaces. However, *Liang* [2000] concluded that spectral reflectance was basically linear from 30 m to 1 km. They averaged the remotely sensed reflectance over 1 km scale. Another study conducted by *McCabe and Wood* [2006] used Landsat (60 m), Advanced Space borne Thermal Emission and Reflection Radiometer (ASTER) (90 m), and MODIS (1020 m) independently to estimate *ETc* over Walnut Creek watershed in Iowa. They further compared these remote sensing estimates against the eddy covariance flux measurements. The Landsat and ASTER-based retrievals were aggregated to MODIS scale to analyze the span of scale from point measurement to MODIS scale and intercompared with aggregated *ETc* estimates. They reported a higher degree of consistency with Landsat and ASTER *ETc* estimates; however, due to heterogeneity in land surface MODIS-based *ETc*, estimates were not consistent with ground measurements.

Long et al. [2011] found that input aggregation of Landsat data to coarser resolution maintain the spatial mean. Since the total number of pixels is reduced in the process of data aggregation, it may change the statistical and spatial characteristic of data; the statistical distribution of the sampled data may deviate from original data set and tends to reduce the spatial correlation at coarser resolution [*Bain*, 1997; *Bian and Butler*, 1999; *Carmel*, 2004]. *Hong et al*. [2009] used simple average and nearest neighbor aggregation methods to up-scale the flux from Landsat 30 m to MODIS 1000 m resolution. They reported that simple average and nearest neighbor aggregation methods preserve the mean value of the original image, however, nearest neighbor aggregation method performed better by preserving the spatial variability of the *ETc*. Studies conducted by *Vieux* [1993], *Zhang and Montgomery* [1994], *Seyfried and Wilcox* [1995], and *Carmel* [2004] pointed out that the data accuracy has been significantly increased by reduction of spatial resolution with respect to original fine-resolution image. On the other hand, some studies also concluded that aggregation to low spatial resolution results in a loss of information that may be valuable for certain applications [*Mo et al*., 2009; *Schoorl et al*., 2000], but some aggregation methods can retain the statistical characteristics of the original data [*Bian and Butler*, 1999]. Despite some studies, the impact(s) of scaling up or scaling down the flux data on the accuracy of *ETc* estimates is not well understood, and the potential variation in *ETc* estimation error with scaling-up or scaling-down process for various surfaces has not been studied sufficiently. The main objectives of this study were: (i) to analyze the ability of Surface Energy Balance System (SEBS) method for Landsat and MODIS satellite to estimate *ETc* over different vegetation surfaces in subhumid/semiarid transition zone in central NE and its validation with ground measurements, (ii) up-scaling/aggregation of Landsat 30 m resolution *ETc* values by simple average, nearest neighbor to larger scales (60, 90, 120, 150, 240, 360, 480, 600, 750, and 1000 m), and (iii) to investigate the effect of aggregation on spatial distribution of energy balance fluxes and potential error associated with the aggregation process.

2. Materials and Methods

2.1. Study Area

The study was conducted in south central Nebraska (Latitude 39°59′39.472″N–41°24′24.80″N and 96°58′37.255″W–98°43′22.815″W (Figure 1)). The total geographical area of the study area is approximately 16,959 km^2 with the statewide-dominant soil type of silt loam soils. The surface elevation varies from 388 m above mean sea level in the south-southeast to 647 m in the north-northwest portion of the state. The study site is in a transition zone between subhumid and semiarid climate with a mean annual and seasonal precipitation of 680 and 470 mm, respectively. The long-term average air temperature ranges from −5°C in January and December to 25°C in July. The land use of the study area is highly heterogeneous and has relatively diverse cropping systems. Land cover classifications of the study region mainly comprise of rainfed and irrigated maize, soybean, sorghum, winter wheat, alfalfa, deciduous forest, grassland, and water bodies (Figure 1).

To evaluate the performance of SEBS, Landsat, and MODIS-derived *ETc*, estimates were first compared with ground measurements obtained from the Bowen Ratio Energy Balance System (BREBS) that have been operating over rainfed grass canopy at location BREBS-3, and winter wheat at location BREBS-3 for 2009. The MODIS-based *ETc* estimates were validated for winter wheat (BREBS-1) and irrigated maize (BREBS-5) locations for 2009. The BREBS-1 is located at the University of Nebraska-Lincoln South Central Agricultural Laboratory (SCAL) near Clay Center, NE. The soil at the BREBS-1 site is well-drained Hasting silt loam with a

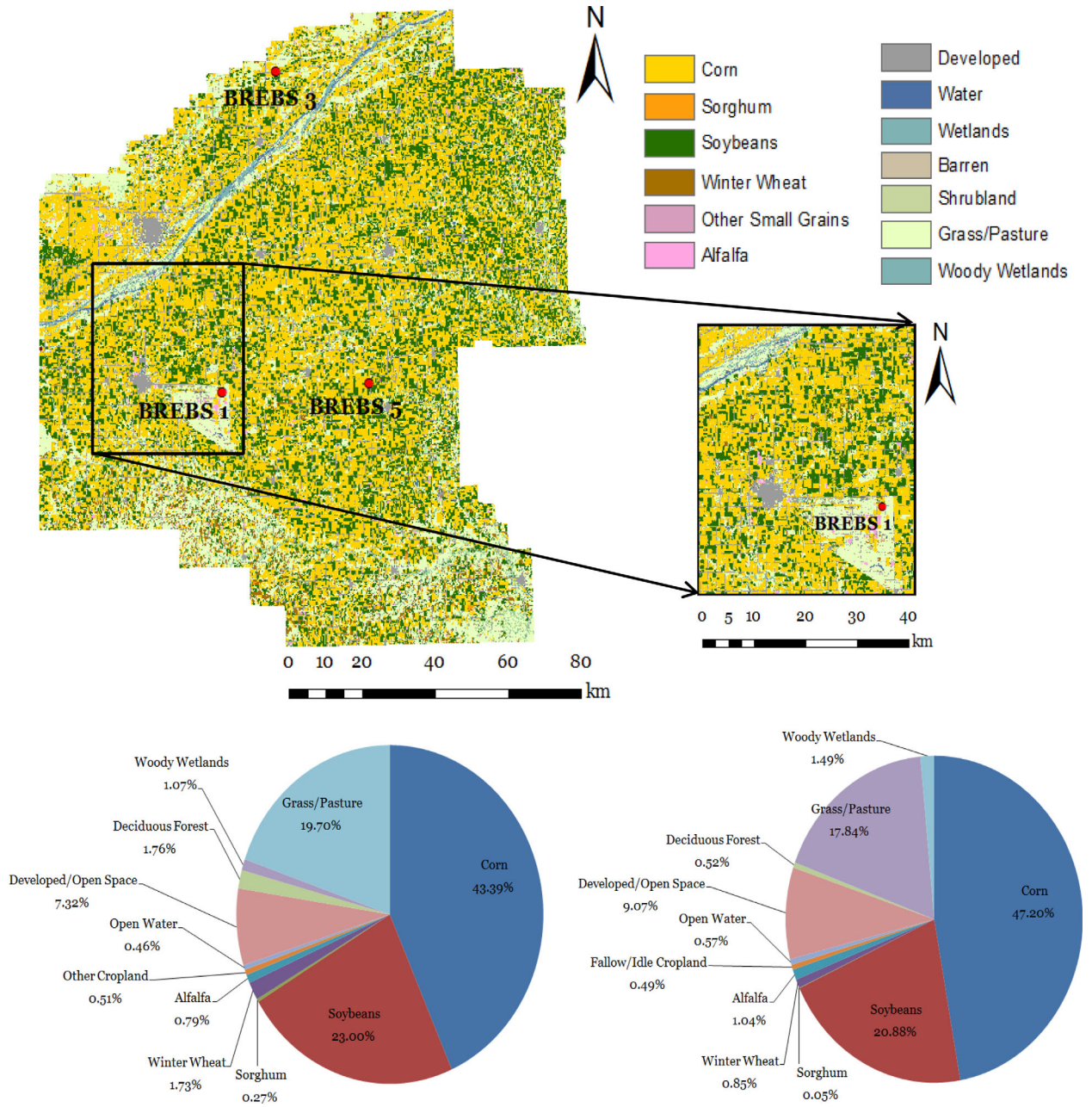

Figure 1. (a, b) Detailed land use map and (c, d) percentage of area of each land use type in south central Nebraska (study area) and small representative area (42 km × 46 km), respectively.

field capacity of 0.34 m^3/m^3 and wilting point of 0.14 m^3/m^3. In 2008, winter wheat was planted on 3 October and was harvested on 9 July. At BREBS-5 location, irrigated maize was planted under no-till conditions. BREBS-3 is a rainfed grassland field of approximately 70 ha in size and contains primarily buffalo grass (*Bouteloua dactyloides* Nutt) and tall fescue. It is a native grassland field established in 1980 [*Irmak*, 2010]. All sites are a part of a larger Nebraska Water and Energy Flux Measurement, Modeling, and Research Network (NEBFLUX) [*Irmak*, 2010] that operates 11 BREB and eddy covariance systems over surfaces ranging from subsurface drip and center pivot-irrigated and rainfed maize and soybean rotation under no-till and disk-till practices; irrigated and rainfed grasslands; irrigated alfalfa; irrigated seed maize/cover crop rotation; phragmites-dominated cottonwood and peach-leaf willow riparian zone; rainfed winter wheat; and other surfaces since 2004. The flux towers measure all surface energy balance components, including latent heat flux (*ETc*), soil heat flux (*G*), sensible heat flux (*H*), and net radiation (*Rn*). Detailed characteristics of the

instrumentation, experimental setup, measurement details, soil and crop and management practices, and other information for each NEBFLUX tower site are provided in *Irmak* [2010]. To study the impact of scaling on *ETc*, smaller representative area 42 km × 26 km at the western part of the study area was selected (Figure 1). Two different dates (30 May and 2 August) during the growing season of 2009 were selected to study the impact of aggregation on *ETc*. On these dates, high-quality and cloud-free images were available. The 30 May 2009 image represents the beginning of the growing season with low vegetation growth while 2 August 2009 images represents the full vegetative cover and is usually associated with the mid-growing season.

2.2. Satellite Data

Cloud-free and geo-rectified for systematic terrain-corrected Landsat 5 (L5) Thematic Mapper (TM), Landsat 7 (L7) Enhanced Thematic Mapper Plus (ETM+), and Moderate Resolution Imaging Spectroradiometer (MODIS) Terra images for the 2009 growing season were used in the analysis. A total of 11 Landsat images for the Path 29-Row 31 and Path 29-Row 32 and 13 MODIS images were used in the analysis. All images were obtained from the Earth Resources Observation and Science Center (EROS), USGS, and NASA Level 1 and Atmosphere Archives and Distribution Systems (LAADS). The scan line correction for L7 band 5 data set was carried out using the neighborhood function with 5 m × 5 m pixel majority function. For both Path 29-Row 31 and Path 29-Row 32 images, neighborhood gap filling technique does not affect the pixels surrounding the BREBS station, as there were no missing pixels. For MODIS image analysis, calibrated radiance (MOD-02) for bands 1–7 at 500 m resolution was used to calculate the radiance and reflectance for bands 1–7. However, band 5 was ignored in the calculation due to systematic striping present in this band 5. MOD-L2 product version 5 was used to calculate the land surface temperature (LST) at the satellite overpass times. This product is further used to calculate net radiation and sensible heat flux in SEBS model. To geo-register the MOD-02 and MOD11-L2 products, MOD-03 geolocation file was used. This file contains the geodetic coordinates, solar zenith angle, and sensor view angle for the images. In the analysis, the maximum sensor view angle of 15° was used to avoid the pixel deformation. The Model Maker Tool of ERDAS imagine processing software (Lecia Geosystems Geospatial Imaging, LLC) was used to code the SEBS algorithms, which subsequently was used to process the Landsat and MODIS images and to check the performance of SEBS algorithms under different vegetation surfaces.

Meteorological data, including hourly air temperature, wind speed, and relative humidity, which were used in SEBS model, were taken from the Clay Center and Central City weather stations, which are part of High Plain Regional Climate Center (HPRCC) Automated Weather Data Network (AWDN). For Landsat images, all images were processed separately for Path 29-Row 31 and Path 29-Row 32 using the weather data from Central City and Clay Center weather stations, respectively, and final *ETc* images were than mosaicked together. The digital number (DN) of the images was converted to top of atmosphere radiance and reflectance values using methodology suggested by *Chander and Markham* [2003] and *Chander et al*. [2007]. In all cases, emissivity and albedo values were calculated using Landsat and MODIS products. The normalized difference vegetation index (*NDVI*) was computed using the infrared (band 4) and red (band 3) band reflectance [*Sobrino et al*., 2004]. Subsequently, the leaf area index (LAI) was calculated from *NDVI* data [*Fisher et al*., 2008] and was used as input for the SEBS model. An iterative procedure was used to calculate the sensible heat flux following the procedures outlined by *Su* [2002].

2.3. Surface Energy Balance System (SEBS)

Surface Energy Balance System (SEBS) [*Su*, 2002] was used for the estimation of surface energy fluxes using satellite data in combination of meteorological data. SEBS model relies on physically based approach as a principle algorithm for partitioning the available energy $(Rn-G)$ between *ETc* and *H* as:

$$\lambda ETc = Rn - G - H \tag{1}$$

where *Rn* is the surface net radiation (W/m^2), *G* is the soil heat flux (W/m^2), *H* is the sensible heat flux (W/m^2), λETc is the latent heat flux (*LE* or actual evapotranspiration, *ETc*; W/m^2), and λ is the latent heat of vaporization (J/kg). In equation (1), the energy for the photosynthesis process and other heat storage terms are considered relatively small and hence neglected. The main input data to the SEBS includes land surface albedo (α), emissivity (ϵ), land surface temperature (T), LAI, and *NDVI*, which were calculated from

spectral reflectance and radiance for both Landsat and MODIS products [*Chander and Markham*, 2003; *Chander et al*., 2007] as mentioned previously. Other inputs consisting of air pressure (*P*), air temperature (*Ta*), relative humidity (*RH*), incoming shortwave radiation (*Rs*), and wind speed at 2 m height (u_2, were obtained from the HPRCC weather stations located at Clay Center and Central City, NE.

One of the main variables used in the land-atmosphere interaction is the *Rn*, which was computed for each pixel as a difference between downward and upward radiation fluxes at the land surface both in shortwave and long-wave domains:

$$Rn=(1-\alpha)*R_{swd}+R_{lwd}-\sigma*\varepsilon*T_s^4-(1-\varepsilon)*R_{lwd} \tag{2}$$

$$Rn=(1-\alpha)*R_{swd}+\varepsilon*R_{lwd}-\sigma*\varepsilon*T_s^4 \tag{3}$$

where, α = land surface albedo, R_{swd} = downward shortwave radiation flux (W/m^2), R_{lwd} = downward long-wave radiation flux (W/m^2), ε = emissivity of the surface, σ = Stefan-Bolzmann constant (5.678 $\times$ 10^{-8} W/m^2/K^4), and T_s = satellite-derived surface temperature.

All components used in radiation balance were calculated using the procedures described in *Su et al*. [1999], *Samani et al*. [2007], and *Vinukollu et al*. [2011]. On a regional scale, *G* is generally not available. Thus, an empirical parameterization of the ground heat flux based on *Rn* and vegetative fraction is used to estimate *G*. Equation developed by *Singh et al*. [2008] and *Irmak et al.* [2011] based on the extensive soil heat flux measurements obtained from NEBFLUX [*Irmak*, 2010] at the University of Nebraska-Lincoln, South Central Agricultural Laboratory (SCAL) near Clay Center, NE, which is a part of our study region, was used in the analysis:

$$\frac{G}{Rn}=(0.3811\exp(-2.3187NDVI)) \tag{4}$$

In SEBS, to determine the evaporative fraction, the actual sensible heat flux was calculated using two limits: (i) sensible heat at wet limit (H_{wet}) and (ii) sensible heat at dry limits (H_{dry}), and the model interpolates the evaporative fraction between these limits. Sensible heat was calculated by Broyden method using the Monin-Obukhov Similarity (MOS) theory [*Monin and Obukhov*, 1954]. Calculation of sensible heat by this method requires the wind speed at near surface (at 2 m height), temperature, and Monin-Obukhov length by simultaneously solving for the stability functions through an iterative process. The wind speed is derived from atmospheric conditions that are characterized by frictional velocity, canopy roughness length, both for momentum and heat transfer at the blending height, which was set to be 200 m for the analysis in this study [*Wang et al*., 2008]. The blending height is defined as the height at which the flow is approximately in equilibrium with local surface and is independent of horizontal position [*Wieringa*, 1986; *Mason*, 1988]. The similarity relationships for the profiles of mean wind speed and mean temperature can be expressed as:

$$u=\frac{u^*}{k}\left[ln\left(\frac{z-d_o}{z_{om}}\right)-\Psi_m\left(\frac{z-d_o}{L}\right)+\Psi_m\left(\frac{z_{om}}{L}\right)\right] \tag{5}$$

$$T_s-T_a=\frac{H}{ku^*\rho C_p}\left[ln\left(\frac{z-d_o}{z_{oh}}\right)-\Psi_h\left(\frac{z-d_o}{L}\right)+\Psi_h\left(\frac{z_{om}}{L}\right)\right] \tag{6}$$

where, *z* is the height above the surface, $u^*=(\tau_o/\rho)^{1/2}$ is the friction velocity, τ_o is the surface shear stress, ρ is the density of air, *k* is von Karman's constant, d_o is the zero plane displacement height, ρ is the air density, C_p is the specific heat of air at constant pressure, T_s is the potential temperature at the surface, and T_a is the potential air temperature at height *z*. The z_{om} is the roughness height for momentum transfer, z_{oh} is the scalar roughness height for heat transfer, Ψ_m and Ψ_h are the stability correction functions for momentum and sensible heat transfer, respectively, which were calculated using *Paulson* [1970] and *Webb* [1970] formulation, and *L* is the Obukhov length, which is defined as:

$$L=-\frac{\rho C_p u_*^3\theta_v}{kgH} \tag{7}$$

where *g* is the acceleration due to gravity, and θ_v is the virtual temperature near the surface. The frictional velocity (u^*) in equations (5) and (6) was calculated as:

$$u* = \frac{ku_b}{\ln\frac{(z_b-d_o)}{z_{om}}-\psi_m} \quad (8)$$

where u_b is the wind speed at blending height z_b, and d_o is the zero displacement height and was determined from the empirical relation given by *Brutsaert* [1982] based on crop height ($d_o = 0.67$ h).

Roughness length of the land surface for momentum transfer z_{om} is a critical variable and determines the height of momentum exchange between the land surface and the atmosphere. z_{om} was calculated considering the height and density using the land use map together with the information provided by LAI and referenced to the associated z_{om} of principle land cover categories of the land use map of Center of Advanced Land Management Information Technology (CALMIT) at the University of Nebraska-Lincoln. Other models have been developed to estimate z_{om} using canopy structure [*Raupach*, 1992, 1995; *Massman*, 1999], but due to unavailability of canopy structure and canopy aerodynamic properties, these models are difficult to apply at regional scales. In remote sensing, z_{om} is often calculated using *NDVI*, which can be derived from energy balance models, however, both the density and height of surface canopy have influence on roughness length, while *NDVI* partly reflect the density of the vegetation canopy [*Su*, 2002]. Roughness height for heat transfer (z_{oh}) is an important parameter in the estimation of heat transfer between the land surface and the surrounding atmosphere. It is a function of surface characteristics, thermal state of the surface, and atmospheric flow, which can be derived as:

$$z_{oh} = \frac{z_{om}}{\exp(kB^{-1})} \quad (9)$$

where kB^{-1} is a dimensionless heat transfer coefficient, which is the inverse Stanton number. In SEBS, an extended model of *Su* [2002] that consists of three terms used to estimate the kB^{-1} as follows:

$$kB^{-1} = \frac{kC_d}{4C_t\frac{u_*}{u(h)}\left(1-e^{\frac{-nec}{2}}\right)}f_c^2 + 2f_cf_s\frac{k\left(\frac{u_*}{u(h)}\right)\left(\frac{z_{om}}{h}\right)}{C_t^*} + KB_s^{-1}f_s^2 \quad (10)$$

The first term in equation (10) physically and geometrically follows the *Choudhury and Monteith* [1988] model for full canopy, the second term accounts for the interaction between the vegetation and soil surface, and the third term is for the bare soil surface value given by *Brutsaert* [1982]. In this equation, C_d is the drag coefficient of the foliage with a value of 0.2; C_t and C_t* are the heat transfer coefficients of the leaf and soil, respectively; n_{ec} is the within-canopy wind speed profile extinction coefficient, f_c and f_s are the canopy and soil fraction coverage, respectively, and $u(h)$ is the horizontal wind speed over the canopy surface (m/s). SEBS used an iterative process to calculate the sensible heat, which was then scaled-up between hypothetical dry and wet limits based on the relative evaporation concept to adjust the sensible heat. After the estimation of sensible heat flux, instantaneous *ETc* was calculated using the scaled *H* between dry and wet limits based on the relative evaporation process [*Su*, 2002; *Su et al*., 2005]. Daily ETc_{24} was then calculated using the average daily *Rn*, daily soil heat flux (assuming $G_{24} = 0$), and evaporative fraction (Λ) :

$$ET_{c24} = 8.54 * 10^7 * \Lambda * \frac{(R_{n24}-G_{24})}{\lambda\rho_w} \quad (11)$$

where, ETc_{24} = daily crop *ET* (mm/d), R_{n24} = daily net radiation (W/m^2), G_{24} = daily soil heat flux (W/m^2), λ = latent heat of vaporization (J/kg), and ρ_w = density of water (kg/m^3).

2.4. Aggregation Process

To understand the consistency in flux estimation at different scale, Landsat-based fluxes were aggregated to 60, 90, 120, 150, 240, 360, 480, 600, 750, 900, and 990 m. Simple average and nearest neighbor resampling techniques were used to examine the influence of choice of aggregation. Simple average resampling procedure calculates the arithmetic mean over an $n \times n$ window. This method smoothes the original values and therefore produce a tighter histogram than the original data. For nearest neighbor, the values of the aggregated pixel are the value from the fine-resolution pixel that lies at the centroid of the coarse pixel. The advantage of nearest neighbor is that unlike simple average, the output values are original input values, and it is easy to compute and fastest to use, however, the output image has rough appearance relative to original image [*Dodgson*, 1997; *Bian and Butler*, 1999; *Hong et al*., 2009; *Ershadi et al*., 2013]. All aggregation

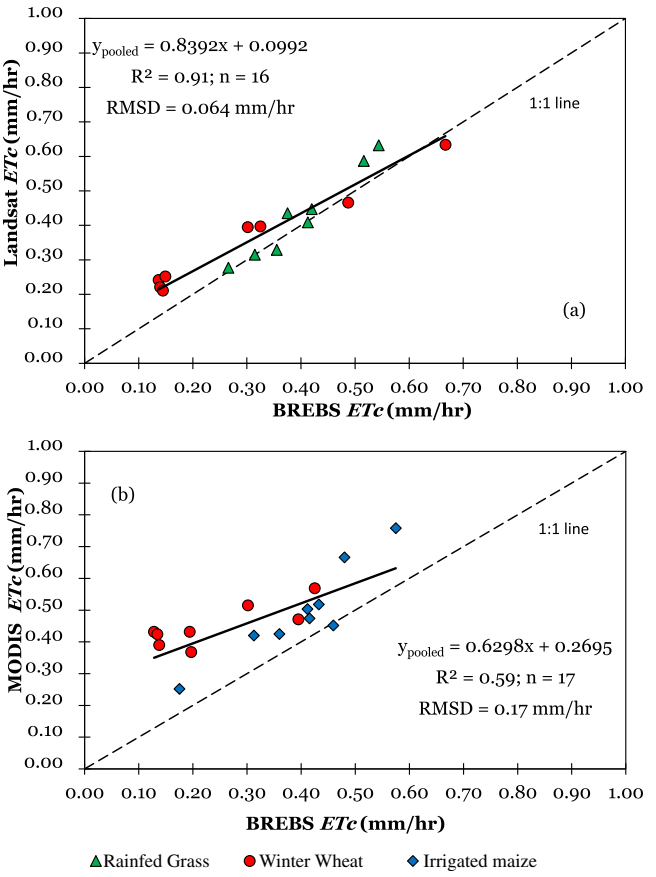

Figure 2. Comparison of SEBS (a) Landsat and (b) MODIS-estimated versus BREBS measured instantaneous crop evapotranspiration (*ETc*, mm/h) for rainfed grass (BREBS-3), winter wheat (BREBS-1), and irrigated maize (BREBS-5) sites (data from NEBFLUX) [*Irmak*, 2010].

techniques were processed in ERDAS Imagine. For up-scaling approach, two methods were adopted. First, the output flux aggregation method was used, where SEBS was applied to the original Landsat image to estimate *ETc* and then aggregating the output flux to low resolution. In second method, the Landsat input radiance was aggregated to low resolution and then processed in the SEBS models. The evaluation of each aggregation method is done by comparing the aggregation results with the corresponding values at the original 30 m resolution at image scale and the field measurement at point scale. For input aggregation described above, only simple average aggregation method is used to up-scale the fine-resolution original radiance product to coarser resolution (MODIS scale). However, for output flux aggregation, simple average and nearest neighbor aggregation methods were used.

3. Results and Discussion

3.1. Measured Versus Estimated Surface Energy Fluxes

A comparison of satellite-based retrievals with ground measurement data offers an imperfect assessment of satellite retrievals because of various influential factors, including the representativeness of the sensor pixel scale, sensor accuracy, and measured versus estimated variables [*Schuepp et al.*, 1990]. In order to check the consistency of SEBS performance for different satellite sensors, SEBS-derived Landsat and MODIS-based *ETc* estimates were first evaluated against *ETc* observations from BREBS towers [*Irmak*, 2010] (Figure 2). BREBS tower records data at 1 h increments, so to validate the satellite-derived ETc at satellite overpass time (11:30 A.M. to 12:00 noon), BREBS tower measurement at 12:00 noon, Central Standard Time (CST) was used in this study. The BREBS approach estimates ETc with its source area determined by the height of the tower and adequate fetch [*Irmak*, 2010]. Fetch was adequate at all the sites. For example, BREBS-1 was installed on a 13.8 ha subsurface drip irrigated field with a fetch distance of 530 m in the north-south direction and about 280 m in east-west direction. The dominant wind direction is usually from south during the summer months in the study sites. Detailed descriptions of the sites, instrumentation characteristics and heights, and measurement details are presented by *Irmak* [2010]. For comparison, the instantaneous value of the surface energy balance flux from SEBS was calculated by averaging the 3 $\times$ 3 pixels (nine 30 m pixels) surrounding the BREBS tower. The validation results were assessed for each of the selected vegetation surfaces (rainfed grassland, rainfed winter wheat, and irrigated maize). The R^2, root-mean-square difference (RMSD), and mean bias error (MBE) were used to assess the error associated with each component. In next step, difference between Landsat (30 m) and MODIS (500 m) satellite sensors were evaluated. Different *ETc* maps were created for two selected dates (30 May and 2 August) in 2009, representing the different growth stages (Figure 3).

In general, a strong correlation with Landsat-based *ETc* estimates and the underlying surface was observed, with patterns of *ETc* strongly related to the land use type (Figure 2a). For Landsat, the comparison of SEBS-estimated and measured *ETc* at the satellite overpass time was made for rainfed grass and winter wheat

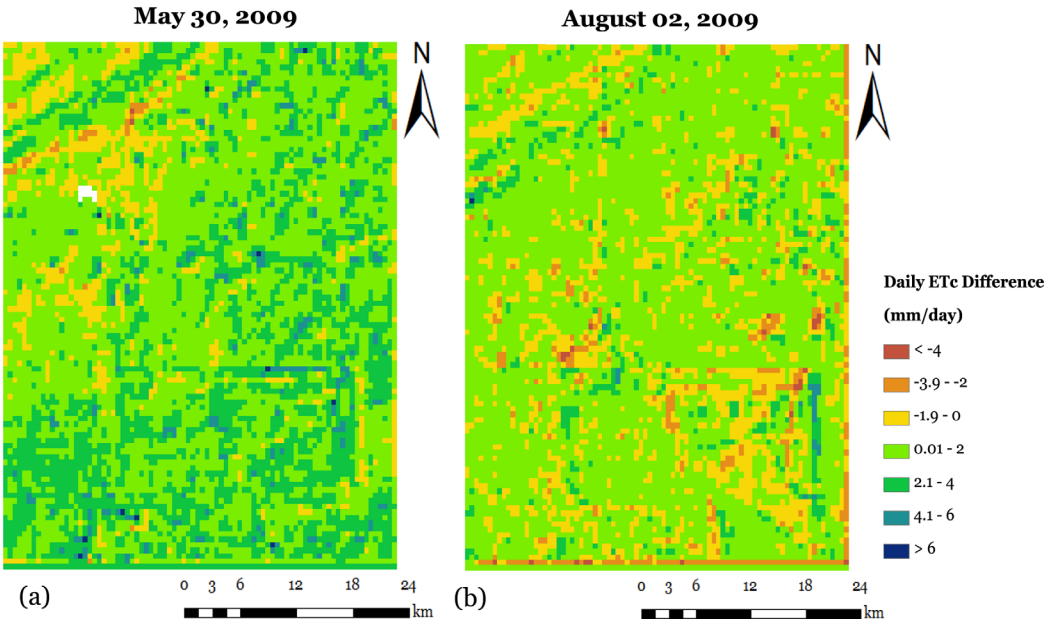

Figure 3. *ETc* difference map between SEBS-derived Landsat (30 m) and MODIS (500 m) on 30 May 2009 and 2 August 2009.

surface. A total of 16 data points were used in the analysis. The regression models explained 91% of the variability in the observed data with RMSD of 0.064 mm/h and MBE of 0.04 mm/h. The variation in *ETc* possibly reflects the different stages of vegetative growth of rainfed grass and winter wheat. When analyzed separately for different vegetative surfaces, higher R^2 of 0.95 (RMSD = 0.05 mm/h; MBE = 0.03 mm/h) and 0.97 (RMSD = 0.07 mm/h; MBE = 0.06 mm/h) was observed between the Landsat SEBS-derived *ETc* with BREBS measurement for rainfed grass and winter wheat, respectively (Table 1). Similar results were observed by *Su* [2002] over the shrubs and grass surface and with RMSD of 82.79 W/m^2 for shrubs and 61.3 W/m^2 for grass. *Ma et al*. [2012] tested the performance of SEBS model using 16 Landsat images over Coleambally irrigation area and reported a good correlation between estimated and observed *ETc* with an $R^2 = 0.95$ (RMSD = 0.74 mm/d) and absolute percent difference of 7.5%.

For comparison, the MODIS-based *ETc* retrievals were validated with the BREBS-1 data for winter wheat surface and BREBS-5 no-till irrigated maize surface (Figure 2b). The comparison between MODIS instantaneous *ETc* estimates versus measured values from BREBS illustrates an imperfect correlation between the two. The regression model explains 59% of the variability in observed *ETc* with higher RMSD of 0.17 mm/h and MBE pf 0.15 mm/h. On an average, MODIS-based *ETc* was 31% higher than the BREBS-measured *ETc*. This difference between the measured and estimated *ETc* may be attribute to the influence of topography and the size of domain (i.e., sensor pixel scale). Similar performance results were reported by other studies. *McCabe and Wood* [2006] reported a general tendency of overprediction by SEBS-based *ETc* estimates using Landsat, ASTER, and MODIS satellite images, and reported a correlation coefficient of 0.71, 0.74, and 0.63, respectively. *Wang et al*. [2006] used surface temperature (*Ts*) versus *NDVI* spatial variation method to estimate evaporative fraction (*EF*) using MODIS products with a bias of −0.002, RMSD of 0.106, and R^2 of 0.61 based on ground observations collected at the southern Great Plains of the United States. Another study used interpolation in the ΔTs-*NDVI* triangular-shaped scatter space to estimate *EF* validated over the North China Plain, using Fengyun-2C data products in combination of MODIS satellite product, reported bias, RMSD, and R^2 of −0.017, 0.14, and 0.55, respectively [*Shu et al*., 2011]. It is important to note that the bias between the observed and estimated *ETc* resulted from numerous factors, such as the underlying surface, growth stage of underlying vegetation, energy balance model assumptions, and ground truth method.

When regression models were developed for individual vegetative surfaces, higher-correlation $R^2 = 0.85$ with RMSD = 0.11 mm/h and MBE = 0.09 mm/h was observed for irrigated maize located at BREBS-5 site (Table 1). Higher correlation may be attributed to the homogeneous surface at the BREBS-5 location (Figure 1). Careful analyses of vegetative surface around BRESB-5 location have showed that most of the surrounding

Table 1. Comparisons Between SEBS-Estimated and BREBS-Measured Surface Energy Balance Fluxes for Landsat and MODIS Satellite for Rainfed Grass, Winter Wheat, and Irrigated Maize[a]

Number	Vegetation	Satellite	*n*	Regression Model	R^2	RMSD (mm/h)	MBE (mm/h)
1	Rainfed grass	Landsat	8	$y_{\text{rainfed grass}} = 1.3105x - 0.0959$	0.95	0.05	0.03
2	Winter wheat	Landsat	8	$y_{\text{winter wheat}} = 0.7499x + 0.1318$	0.97	0.07	0.06
3	Irrigated maize	MODIS	9	$y_{\text{maize}} = 1.1956x + 0.0152$	0.85	0.11	0.09
4	Winter wheat	MODIS	8	$y_{\text{winter wheat}} = 0.445x + 0.3437$	0.65	0.22	0.21

[a] *n* = number of observations (images); R^2 = coefficient of determination; RMSD = root-mean square difference.

fields are also of maize and soybean at similar growth stage. This homogeneity in land use at BREBS-5 location results lesser bias in *ETc* measurement at 500 m MODIS resolution. However, at BREBS-1 location, the correlation between the measured and MODIS estimate shows an average relationship with $R^2 = 0.65$ (RMSD = 0.22 mm/h and MBE = 0.21 mm/h). At BREBS-1 location, the MODIS-based *ETc* was about 53% higher than actual BREBS measurement. The higher bias at BREBS-1 location may be due to complex terrain, resulting in heterogeneity of the landscape surrounding winter wheat field in 2009 and the pixel area extends beyond the scale of the field under consideration and covers the surrounding fields. Most of the surrounding fields were maize, soybean, and alfalfa (Figure 1). Furthermore, at the end of the May, winter wheat had full canopy cover and greater water use (between booting and flowering stages). However, water use starts decreasing after flowering stage and approximately 4 weeks after peak water use, winter wheat reaches its full physiological maturity and is usually ready to be harvested. At the same time, maize and soybean in surrounding fields were just planted or emerged, with low *ETc* values. This heterogeneity in land covers at BREBS-1 at 500 m resolution appears to create more bias in the final estimation of *ETc* from MODIS satellite under the conditions studied. A heterogeneous surface influences the surface optical properties (albedo and emissivity), the fraction of absorbed photosynthetically active radiation, the transpiration rate, and surface energy budgets [*Guillevic et al*., 2012]. For example, at the BREBS-1 location, winter wheat field is surrounded by other vegetation, and resulted in a higher temperature difference, and hence in an overestimation of *ETc*. It is also important to note that the *ETc* estimates derived from Landsat and MODIS depend on the uncertainty and bias from models itself (SEBS in this study) as well as measurement uncertainty of the model inputs. Comparison between the spatial distribution of *ETc* from Landsat and MODIS sensors versus BREBS *ETc* clearly suggested the inability of MODIS sensor to accurately characterize fluxes due to coarser resolution. However, the high temporal resolution of MODIS satellite can provide valuable data for assessing the current land cover and land use changes.

To investigate the spatial variation in Landsat and MODIS-based *ETc* over heterogeneous surfaces, two scenes of Landsat and MODIS imagery representing different growth stages were selected in 2009 (30 May 2009 and 2 August 2009) and difference maps were created. Difference map refers to pixel-by-pixel difference between Landsat and MODIS *ETc* estimates (Figure 3). Brown color pixel represents the location where MODIS-derived *ETc* was greater than Landsat-derived *ETc* and blue color pixel represents where Landsat-based *ETc* was greater. Basic Statistics (mean and standard deviation (SD)) allow quantitative means of comparison and evaluation. Positive and negative differences between two images tend to cancel each other in these calculations since they occur in opposite direction. Therefore, mean and SD of each difference images were calculated based on the absolute difference between Landsat and MODIS-based *ETc*. On an image scale, the average absolute difference of 1.04 mm/d (SD = 0.85 mm/d) and 1.03 mm/d (SD = 0.77 mm/d) was observed on 30 May 2009 and 2 August 2009, respectively. On 30 May 2009, the majority of the area had between 0 and 2 mm/d or higher difference, representing higher Landsat-derived *ETc*. However, in northwestern part of the image along the Platte River, MODIS-derived *ETc* was higher than Landsat-based *ETc* (negative difference) due to mixed pixel across that area. Higher positive difference at central and southern part of the image might be due to under estimation of SEBS-derived *ETc* for MODIS sensor because of homogeneity of land use across that area. On 2 August 2009, about 80% of the total image area had 0–2 mm/d difference, with some areas showing higher MODIS-derived *ETc* as compared to the Landsat-based *ETc* (Figure 3, green color). These higher and lower *ETc* differences might be due to the combination of subtraction of larger pixel *ETc* values from the Landsat 30 m based pixel, mixed pixel across the image, and disagreement in image georeferencing between Landsat and MODIS images. In general, the satellite image has a geo-referencing difference of a size of one or two pixels which can cause abrupt changes in *ETc* at the boundaries as was also observed by *Eugenio and Marqués* [2003] and *Hong et al*. [2009]. Also,

geo-referencing match between images from different satellite sensors produce more error than those obtained from the same sensors. Results presented in this study are consistent with *Hong et al*. [2009], they reported the absolute difference map between Landsat (30 m) and MODIS (250 m) images near Middle Rio Grande Basin for 16 June 2002 and 14 September 2002. Their results stated that the larger difference pixels between over the study area were due the difference in spatial resolution between Landsat and MODIS sensors and surface heterogeneity over the study area.

3.2. Aggregation Effect

A common practice to analyze the effect of scaling behavior over the heterogeneous surfaces is to aggregate the fine-resolution data to coarser solution [*Kustas et al*., 2004]. Due to heterogeneity, one intuitively expects that the limit of flux discrimination should approach the dimensions of the average field [*McCabe and Wood*, 2006]. To understand this, Landsat images were aggregated to larger scales of 60, 90, 120, 150, 240, 360, 480, 600, 750, 900, and 990 m. Spatial distribution and its statistical features (histogram) were evaluated and compared among different aggregation procedures both on image and pixel scale. In output aggregation, SEBS-derived Landsat 30 m *ETc* product was aggregated to coarser resolution using simple average and nearest neighbor resample techniques. The resultant aggregated *ETc* map may represent the best estimate of *ETc* at the coarser resolution, since the aggregated *ETc* was derived directly by aggregation of the fine-resolution *ETc* data. In input-aggregation, Landsat input radiance was aggregated to coarser resolution and then processed in the SEBS models to calculate *ETc*. A small representative area of 42 km $\times$ 46 km was selected from the study area, which contains 1601 $\times$ 1401 pixels ($n = 2{,}243{,}001$) for Landsat and 85 $\times$ 97 ($n = 8245$) pixels for MODIS scale to evaluate the effect of resolution on *ETc* estimates. Following sections discuss the spatial variability, basis statistics, and error associate in *ETc* and associated components at aggregated resolutions.

3.3. Output Aggregation Effect

3.3.1. Image-Scale Error

To study the impact of output aggregation on *ETc* retrievals at image scale, SEBS-derived Landsat-based *ETc* at 30 m pixel resolution was aggregated to a coarser resolution using simple average and nearest neighbor aggregation methods. The spatial distribution of daily *ETc* was evaluated and compared for two aggregation methods across five different resolutions (30, 120, 240, 480, and 990 m). These resolutions were selected as 240, 480, and 990 m which are closest to the nominal 250, 500, and 1000 m resolution of MODIS 8 day average MODIS (MOD-09), radiance (MOD-02), and daily Land surface temperature (MOD11-A1) products, respectively. However, for statistical analysis and evaluation of the aggregation transfer errors associated with the aggregation, additional resolutions of 60, 90, 150, 360, 600, 750, and 900 m were also used in the analysis. The spatial variation of *ETc* at aggregated resolutions along with histogram analysis and descriptive statistic using simple average and nearest neighbor resampling techniques were analyzed on 30 May 2009 and 2 August 2009 (Figures 4 and 5). These dates were selected to represent two different growth stages: one at the beginning of the growing season (30 May 2009) and other when plants had full canopy closure (2 August 2009). Spatial distribution of *ETc* clearly shows high transpiration rate on 2 August 2009 (about 90% of the image area) relative to 30 May 2009. At this time of the year, maize and soybean (predominant cropping systems in the study area) are usually in the middle of the growing season and crop reach their full canopy cover with substantially greater *ETc* rates, with daily average rate of 7.81 mm/d (SD = 2.04 mm/d). In May image, higher *ETc* rates were mostly observed in alfalfa fields and the riparian vegetation along the Platte River in the north-west part of the image. At this time of the year, maize and soybean (predominant cropping systems in the study area) are usually at the beginning stage of the growing season and transpiring at low rates. On an image scale, the average *ETc* of 3.96 mm/d (SD = 2.05 mm/d).

Even though there is significant loss of spatial detail with the increase in resolution, the overall spatial distribution of *ETc* over aggregated scales were consistent with the original Landsat 30 m *ETc*. For both simple average and nearest neighbor resampling methods, the frequency of histogram distribution decreases with the increase in the spatial resolution. However, with simple average aggregation method, there is change in the shape and pattern of the histogram at coarser resolution as compared to the nearest neighbor method. On 30 May 2009, the histogram peaked at 2.58, 2.62, 2.66, and 2.62 mm/d at 30, 120, 240, and 480 m resolutions, respectively; however, this peak shifted toward higher *ETc* of 3.29 mm/d at 990 m resolution when aggregated using simple average aggregation. At 990 m pixel resolution, the frequency of the pixels having

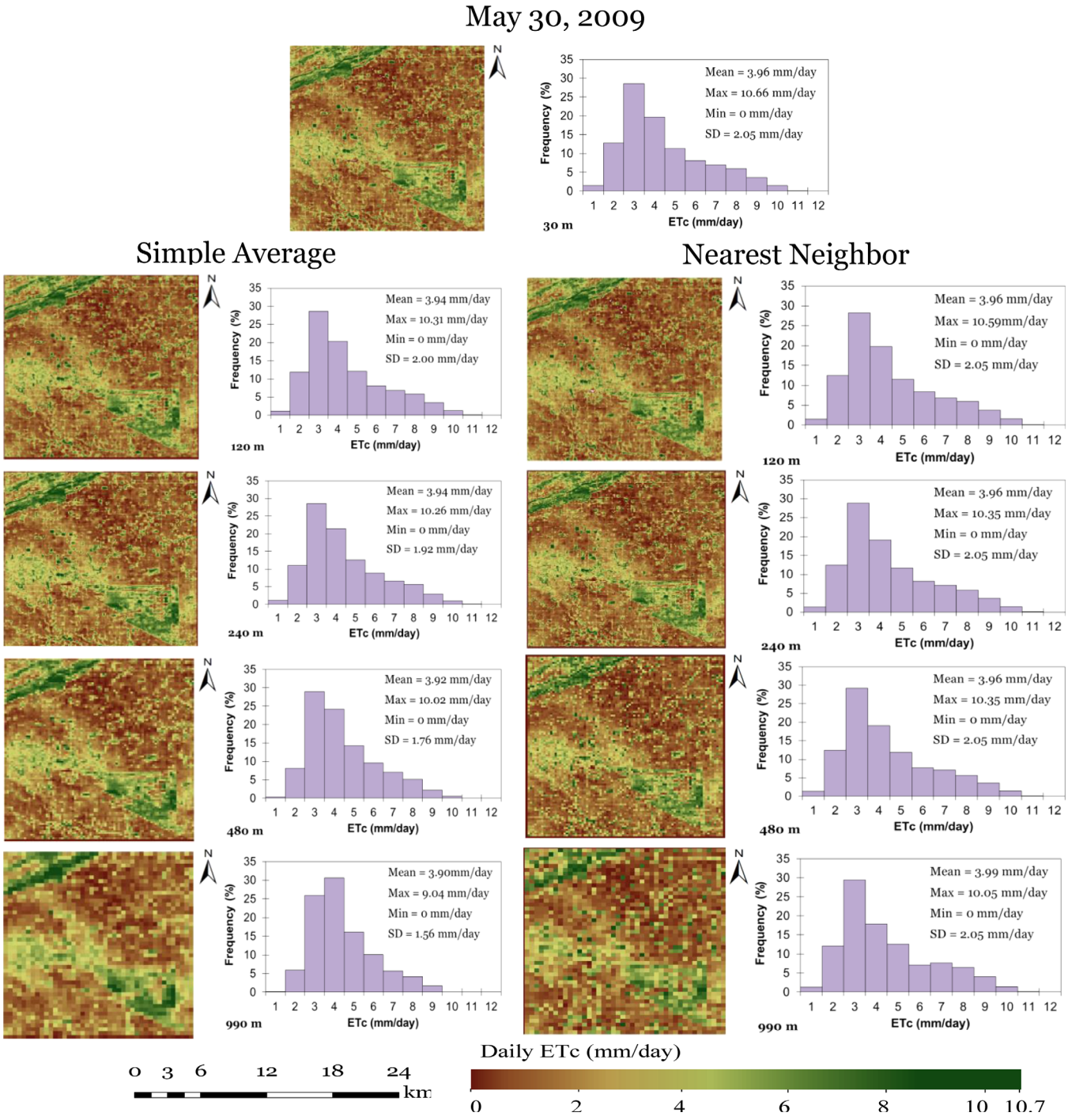

Figure 4. Spatial variation of *ETc* along with histogram distribution (bin size = 1 mm/d) of original 30 m Landsat image and at aggregated spatial resolution of 120, 240, 480, and 990 m from output flux up-scaling on 30 May 2009 using simple average and nearest neighbor resampling technique.

2–3 mm/d *ETc* decreased, but the frequency of the pixels having 3–4 mm/d *ETc* increased when using simple average resampling technique. This shift in the peak value might be due to the mixed pixels across the Platte River and near the USDA Meat Animal Research Center land area near Clay Center, NE.

At higher resolution, the low *ETc* pixels were easily mixed with the high *ETc* pixels when applying the simple average aggregation method. However, no change in histogram peak was observed when aggregated using nearest neighbor aggregation resampling method since nearest neighbor preserve the original data.

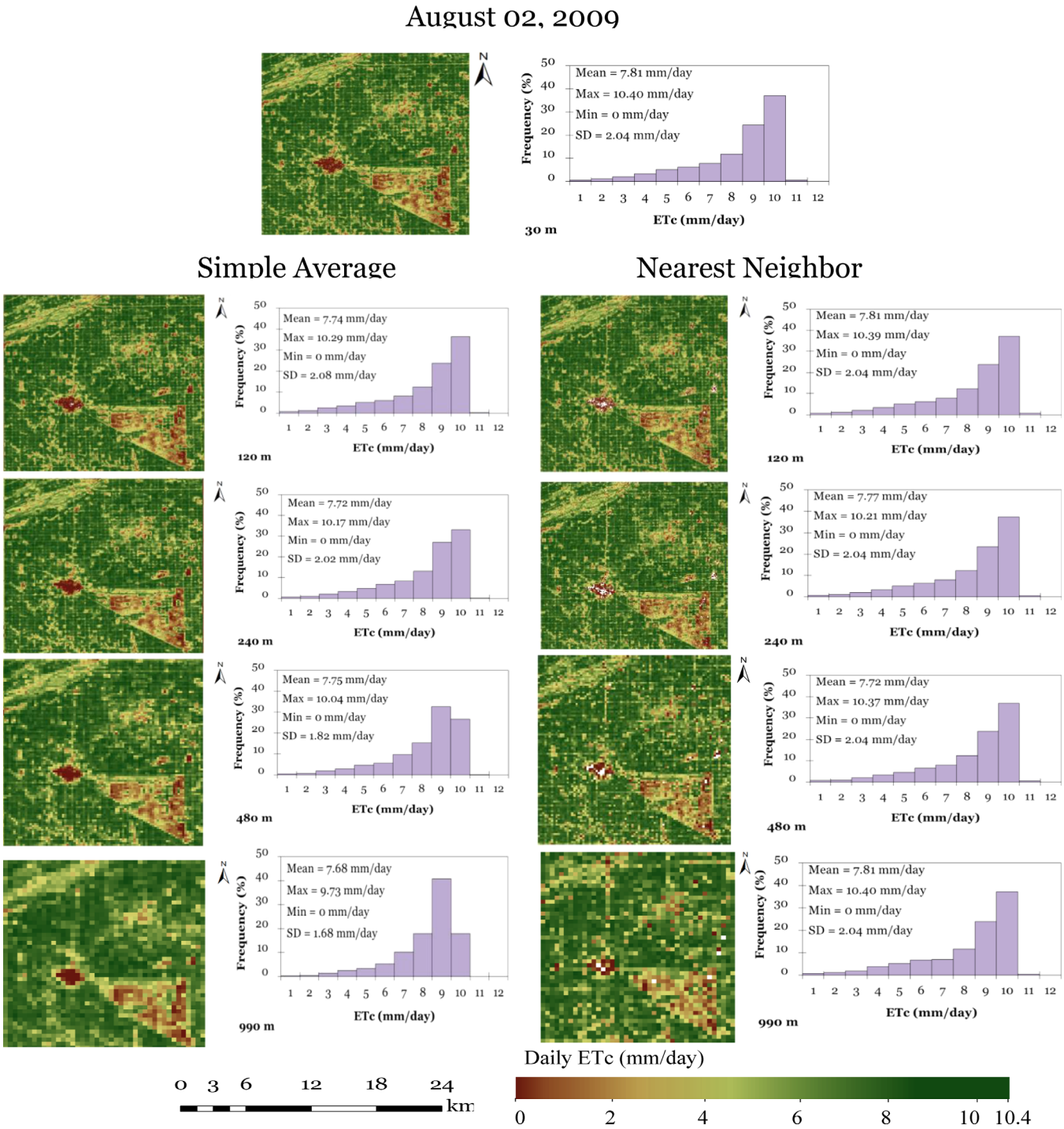

Figure 5. Spatial variation of *ETc* along with histogram distribution (bin size = 1 mm/d) of original 30 m Landsat image and at aggregated spatial resolution of 120, 240, 480, and 990 m from output flux up-scaling on 2 August 2009 using simple average and nearest neighbor resampling technique.

The peak of histogram on 30 May 2009 using nearest neighbor aggregation method was between 2.3 and 2.6 mm/d. Similar observation existed on 2 August 2009, with *ETc* values more skewed toward higher *ETc* values. The peak *ETc* on 2 August 2009 was in the range of 9–10 mm/d; however, this peak changed to 8–9 mm/d at 480 and 990 m spatial resolution when aggregated using simple average resampling technique. Similar to 30 May 2009 *ETc* distributions, no change in the histogram pattern was observed when aggregated using the nearest neighbor resampling method, with peak of the histogram being in the range

of 9–10 mm/d (Figure 5). The histogram distribution is positively skewed toward low *ETc* rates; however, for image with higher *ETc* values, the peak of the histogram distribution moved to lower *ETc* values when resampled using simple average aggregation method. These results are consistent with those reported by *Ershadi et al*. [2013] who observed that the peak of *ETc* values vary with each aggregated resolution. They suggested that this difference is due to the difference in SEBS and SEBAL (Surface Energy Balance Algorithm for Land) models to predict *ETc* and difference in land use/land cover conditions. However, *Hong et al*. [2009] observed that the peak of the histogram of *ETc* increased by 10–15% with simple average aggregation. The ranges of *ETc* for both resampling methods vary with aggregation resolution; however, the mean values of the resampled images approximately remain the same across all resolutions for both days. Maintaining the consistency in mean spatial flux is important at MODIS level resolution, since the ability to identify crop specific distribution is limited when the length scale of the surface heterogeneity is less than the sensing resolution [*McCabe and Wood*, 2006]. The SD decreased when resampled using simple average aggregation with a total reduction of 24% and 18% from 30 to 990 m spatial resolution on 30 May 2009 and 2 August 2009, respectively. However, no change was observed in SD values for nearest neighbor method. The nearest neighbor resampling method is based on the location of the central pixel, which changes with the increasing pixel size, hence the values of resampled image remain restricted to the original image, which result in the blocky pattern at coarser resolution. Similar reduction in SD by simple average resampling approach was observed by *Hong et al*. [2009] who reported reduction of 9.7% and 9.0% from 30 to 1000 m resolution, respectively. Many hydrological process models require input parameters over a large area. On regional scale, direct averaging technique of input variables has often been used to generate the regional-scale model input parameters [*Croley et al*., 2005; *Maayar and Chen*, 2006]. However, it is important to note that the SD of the data set decreases with aggregated resolutions, therefore, users need to check the sensitivity of the range of the input variables of the model prior to applying direct averaging for data aggregation.

3.3.2. Pixel Scale Error

To quantify the error associated with the output flux aggregation at pixel scale, each aggregated pixel was compared to the original 30 m pixel located within; e.g., pixel values of each aggregated resolution were compared to the $n \times n$ set of 30 m pixels from which it is comprised of. The mean absolute difference and percent relative mean difference were calculated at each resolution as compared to the original Landsat image on 30 May 2009 and 2 August 2009 (Table 2). Absolute difference values were calculated by subtracting the aggregated *ETc* values from original (native) Landsat 30 m *ETc* values and percent relative difference values were calculated by dividing the absolute difference by the native 30 m Landsat *ETc* values. For all cases, mean absolute difference and SD increased with the pixel size due to the mixed pixel effect of underlying heterogeneous surface. Since aggregation tends to average out the small surface features, the difference between aggregated imagery and the original fine-resolution imagery increases with aggregation levels. The absolute mean difference for simple average and nearest neighbor aggregated methods on 30 May 2009 ranged from 0.24 mm/d (SD = 0.18 mm/d) to 1.13 mm/d (SD = 0.61 mm/d) and 0.29 mm/d (SD = 0.40 mm/d) to 1.35 mm/d (SD = 0.88 mm/d), respectively. Slightly higher differences were observed on 2 August 2009 for both up-scaling approaches (Table 2) which can be explained by much higher *ETc* rate in the August image than those in May. For both days (May and August), higher percent relative difference was observed for the nearest neighbor aggregation method with a maximum of 34% and 20% at 990 m resolution, respectively. This implies that simple average resample method can generate less error at pixel scale and can be used for aggregation purpose. Mean relative error between up-scaled image using simple average and nearest neighbor resampling method at 480 and 30 m original Landsat image were also compared with the mean relative difference between original Landsat and MODIS image at 500 m spatial resolution. On average, a small difference was observed for both resampling methods on 30 May 2009 and 2 August 2009, respectively. Similar results were observed by *Moran et al*. [1997] who reported small change in land surface temperature, but larger error associated with sensible heat flux at coarser resolution over a heterogeneous surface. Another study conducted by *Su et al*. [1999] observed the error of 10–30% in evaporative fraction when aggregated to 1184 m.

3.4. Input Aggregation Effect

3.4.1. Image-Scale Error

In input aggregation procedure, the Landsat input radiances were aggregated to lower resolution, from 60 to 990 m, and then processed in the SEBS model. No difference in *ETc* was observed between output and

Table 2. Output Flux Aggregation Pixel-by-Pixel Scale Absolute Mean Difference, Standard Deviation (SD), and % Relative Difference Between Landsat (30 m) and Simple Average and Nearest Neighbor Aggregated *ETc*

Simple Average				Nearest Neighbor			
Resolution (m)	Mean Difference	SD	% Mean Relative Difference	Resolution	Mean Difference	SD	% Mean Relative Difference
30 May 2009							
60	0.24	0.18	6.1	60	0.29	0.40	7.4
90	0.25	0.23	6.3	90	0.26	0.38	6.7
120	0.33	0.28	8.3	120	0.50	0.61	12.5
150	0.47	0.37	11.9	150	0.53	0.69	13.5
240	0.60	0.47	15.2	240	0.80	0.63	20.2
360	0.64	0.49	16.2	360	0.95	0.68	24.0
480	0.96	0.58	24.2	480	1.00	0.71	25.4
600	1.03	0.54	26.0	600	1.01	0.77	25.6
750	1.06	0.50	26.7	750	1.12	0.80	28.3
900	1.10	0.48	27.7	900	1.16	0.83	29.4
990	1.13	0.61	28.5	990	1.35	0.88	34.1
2 August 2009							
60	0.28	0.21	3.6	60	0.31	0.48	3.91
90	0.32	0.24	4.1	90	0.27	0.38	3.45
120	0.36	0.32	4.6	120	0.52	0.53	6.70
150	0.41	0.36	5.2	150	0.55	0.67	7.08
240	0.63	0.52	8.1	240	0.86	0.71	10.98
360	0.77	0.51	9.9	360	1.03	0.69	13.16
480	1.05	0.64	13.4	480	1.09	0.80	13.91
600	1.08	0.63	13.8	600	1.11	0.79	14.24
750	1.12	0.55	14.3	750	1.20	0.83	15.40
900	1.19	0.60	15.2	900	1.28	0.88	16.39
990	1.23	0.69	15.7	990	1.54	0.91	19.75

input aggregation when applying nearest neighbor. Hence for this study, only simple average resampling method was used to aggregate Landsat 30 m radiance. To examine the impact of scale, the key input used in the SEBS model such as *NDVI*, surface temperature (*Ts*), and sensible heat flux (*H*) were also analyzed at each aggregated resolution and influence of the aggregated input on flux retrieval were discussed. The loss of spatial pattern with decreasing spatial resolution was considered as the error associated between original Landsat images (30 m) and the coarser resolution image. The loss of spatial detail is evident with the aggregation from 30 to 990 m; however, the loss of significant spatial detail is apparent from 240 to 990 m. At 990 m pixel resolution, the spatial variability in *NDVI*, *Ts*, *H*, and *ETc* images were dramatically reduced and spatial structures in the landscape are obscured (data not shown).

Relative spatial mean values at each aggregated pixel resolution for *NDVI, Ts*, *Rn*, *H*, and *ETc* for 30 May 2009 and 2 August 2009 images were quantified (Figure 6). The relative spatial mean was calculated by dividing the aggregated values by the original 30 m Landsat values. On 30 May 2009, no change in *NDVI* values was observed at aggregated resolution. On the other hand, small change was observed on 2 August 2009 and this increase is more evident at spatial resolution of 240 m and coarser resolutions. This increase is due to the high values of *NDVI* on 2 August 2009 showing the effect of land cover on *ETc*. The relative spatial mean for *Ts* increases with spatial resolution on both days. This increment in *Ts* results a small increase in *Rn* on 30 May 2009; however, on 2 August with the increase in relative spatial mean for *Ts*, a decline was observed in *Rn*. The variation in *Rn* over the aggregated scales represents the variation of aggregated albedo and emissivity values that have an effect on image-scale average value of *Rn*. Similar small increasing and decreasing trend was observed in *G* on 30 May and 2 August (*G* was calculated using the empirical relation (equation (4)) using *NDVI* and *Rn*).

The relative spatial mean value for *H* decreased with increasing resolution on 30 May 2009 as compared to increasing trend on 2 August due to the combined effect of wind speed and aggregated roughness properties of the surface (z_{om} and z_{oh}) on both dates. Wind speed and air temperature used in the SEBS model are constant over the study region; however, land surface parameters are derived using Landsat image, and using the SEBS model can cause the variability in *H*. This relative spatial mean difference in *Rn* and *H* with the resolution results in the final increasing or decreasing trend in *ETc*. Opposite to *H*, a decreasing and increasing trend in *ETc* was observed on 30 May 2009 and 2 August 2009, respectively. However, the magnitude of change in *H* and *ETc* was not the same on both days due to contribution of other factors used to calculate *ETc*.

3.4.2. Pixel Scale Error

To evaluate the effect of input flux aggregation at pixel scale, each pixel value of aggregated resolution was compared to the $n \times n$ set of 30 m pixels from which it is comprised of. Mean absolute difference and percent relative mean difference were calculated for each case and the pixel scale errors in *NDVI*, *Ts*, *Rn*, *H*, and *ETc* at each aggregated resolution are presented in Figure 7. For both dates, relative error in *Ts* and *Rn* was

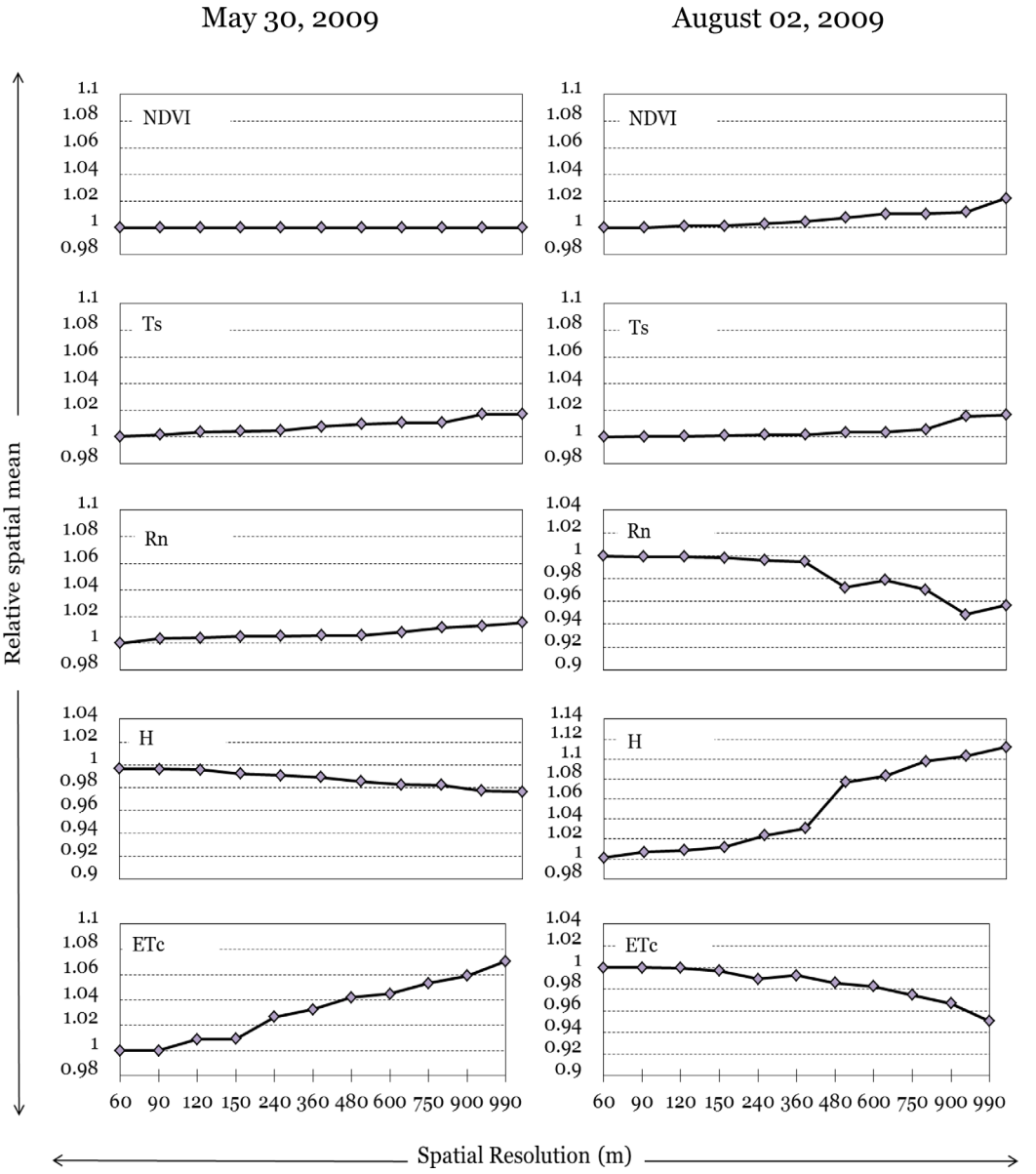

Figure 6. Image-scale relative spatial mean for *NDVI*, land surface temperature (*Ts*), net radiation (*Rn*), sensible heat (*H*), and daily crop evapotranspiration (*ETc*) at input aggregated spatial resolutions on (a) 30 May 2009 and (b) 2 August 2009.

less than 10%. Pixel scale percent relative error ranged from 10% for 60 m resolution to 30% for 990 m resolution for *NDVI* on both dates. Higher pixel scale relative error was observed in *H* and *ETc* with maximum error of 42% observed in *ETc* as compared to 25% in *H* on 30 May 2009. On an average, with every increase in 30 m resolution, percent relative error increase by 0.82, 0.02, 0.50, 0.22, and 0.47% for *ETc*, *Ts*, *H*, *Rn*, and *NDVI*, respectively. However, on 2 August, higher relative error of 60% was observed in *H* compared to 26% in *ETc*. Contrary to 30 May, lower range of 30% incremental error was observed on 2 August 2009 in all cases expect *H*. The average increase of 0.44, 0.03, 1.36, 0.09, and 0.23% was observed for *ETc*, *Ts*, *H*, *Rn*, and *NDVI* with every 30 m increase in spatial resolution from 30 to 990 m, respectively. This higher error in *H* might be due to the difference in surface roughness parameters on both the dates at aggregated resolution. The spatial distribution (not shown) of relative error for *H* and *ETc* illustrated that the errors were related to the variation in land-use/land cover characteristics. Higher error in *H* and *ETc* corresponds to transition zones, such as area near Platte River riparian zone, roads and transition zones between the agricultural fields and

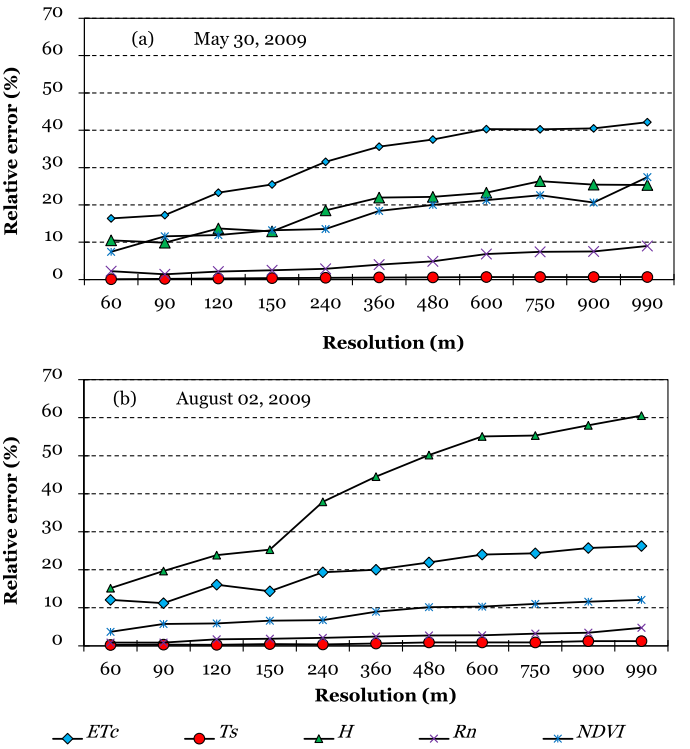

Figure 7. Pixel scale percent relative error for *NDVI*, surface temperature (*Ts*), net radiation (*Rn*), sensible heat flux (*H*), and daily crop evapotranspiration (*ETc*) across input aggregated spatial resolutions on (a) 30 May 2009 and (b) 2 August 2009.

near cities, where land surface changes with the pixel scale (Figure 1). Higher error was observed in *H* and *ETc* as compared to the *Rn* and *Ts*, which indicates the importance of aerodynamics resistance parameterization in flux estimation, which is related to the surface roughness components (z_{om}, z_{oh}) at aggregated scales. Careful analysis has shown that the mean and standard deviation of absolute difference and relative difference from output up-scaling with the simple averaging map are smaller than the one from input up-scaling (Table 2 and Figure 7). Also, the simple averaging method generates smaller absolute difference and relative difference than the nearest neighbor method. This implies that the *ETc* of the original Landsat images seems to be better preserved with output up-scaling than with input up-scaling. Also, it is also important to note that the mean aggregated *ETc* at different resolution using the output flux aggregation procedure does not equal to the ETc values obtained from the input aggregation at same resolution due to nonlinearity in SEBS algorithm [*Su*, 2002]. For example, slightly higher error was observed in case of input upscaling using simple average from output aggregation with simple average. Results presented here are consistent with *Ershadi et al*. [2013], they reported low pixel scale relative error of less than 5% for *Ts* and available energy (*Rn* – *G*). However, for *ETc*, they reported relative error ranging from 20% to more than 40% at 960 m spatial resolution for *ETc* due to decrease in aerodynamic resistance at coarser resolution, which originates from the change in the roughness length parameters of the land surface due to aggregation. *Moran et al*. [1997] reported a higher error of $\geq$50% in *H* when aggregated to low resolution. They reported that error in aggregation of *H* was highly influenced by the heterogeneity of the land surface characteristics.

3.5. Scaled-Up MODIS *ETc*

In order to evaluate the performance of up-scaled image using simple and nearest neighbor resampling method, we compared the up-scaled aggregated *ETc* image at 480 m pixel resolution with the original SEBS-derived MODIS *ETc* at 500 m spatial resolution. Comparisons were made with the output flux aggregation using both resampling technique and input flux aggregation for simple average for 2 August 2009 image. Lower mean absolute difference and relative difference of 1.04 mm/d (SD = 0.76 mm/d) and 13.4%, respectively, were observed for simple average output up-scaled *ETc* image with the original MODIS image at 500 m resolution. On the other hand, higher difference of 1.53 mm/d (SD = 0.95 mm/d) and relative difference of 20% were observed when compared with the nearest neighbor resampling method. Comparison with input aggregated image using simple average revealed a larger difference of 1.56 mm/d and relative error of 22%. No difference between output and input up-scaling is found from the nearest neighbor aggregation method. Our results indicate that the output aggregation using simple average aggregation method provide closer representation of *ETc* at 500 m MODIS pixel resolution than the nearest neighbor resampling method.

4. Summary and Conclusions

Significant progress has been made over the past two decades in satellite-based *ETc* monitoring where it is operationally and economically feasible in providing large-area *ETc* information at accuracies and spatio-temporal resolutions required for many practical water resource applications. However, spatial resolution of remotely sensed *ETc* and other energy balance fluxes depends on the specification of satellite sensors, for example, satellite-based flux retrievals is tempered by the frequency of their return rate. For practical purposes (i.e., irrigation scheduling/water allocation), high-resolution ETc image (e.g., Landsat) can provide adequate information, but in many cases are not easily available due to low temporal variability, cloud cover, and high costs. On the other hand, an estimate of a daily *ETc* from MODIS cannot consider the heterogeneity of land surface characteristics, which may result in potential error in flux estimation. However, MODIS would provide an extremely valuable data source for assessing current land and vegetation states at regional scale. Therefore, it is crucial to understand the implications of coarse resolution retrieval of surface energy fluxes relative to fine-resolution responses.

This study highlights the impact of spatial scaling of evapotranspiration and other energy balance fluxes using Landsat and MODIS images over heterogeneous surfaces in south central NE. Following the validation of Landsat and MODIS *ETc* retrievals with measured ground data, a detailed analysis of input and output up-scaling of surface energy balance fluxes from 60 to 990 m using simple average and nearest neighbor was performed. It was observed that Landsat has more preferable spatial resolution (30 m) to map and analyze *ETc* compared to MODIS (500 m), with regression model explaining 91% and 59% of the variability on BREBS-measured *ETc*, respectively. Pixel-by-pixel comparisons showed an absolute difference close to 1 mm/d. This difference is mainly due to the underlying assumption of spatial heterogeneity, difference in spatial, spectral and radiometric resolution between the Landsat and MODIS sensors. Aggregation results revealed that the influence of output and input aggregation underestimate the *ETc* at coarser resolutions as compared to original high-resolution Landsat image at 30 m resolution. Among all aggregation approaches, output aggregation using simple average performed better than nearest neighbor by preserving both the spatial distribution and the magnitude of *ETc* at the image (relative error $< 10\%$) and pixel scales (relative error 5–35%). Spatial variation of relative error illustrate that the larger relative error mainly occurred at transition zones, such as area near the Platte River, roads and transition zones between the agricultural fields and near cities, where land surface changes with the pixel scale. Our analysis illustrated larger error associate to the input up-scaling (relative error = 25–60%) as compared to output up-scaling using simple average aggregation approach. It was observed that the higher error was due to the changes in land surface characteristics such as changes in roughness height parameters across aggregated resolution in SEBS model. Comparison of aggregated *ETc* images and original MODIS image (500 m) revealed that simple average aggregation method provided a closer representation of *ETc* values at MODIS pixel resolution than the nearest neighbor resampling method.

The results presented here illustrate the error propagation in flux retrieval with the decrease in spatial resolution and difference in land use characteristics. Land surface heterogeneity is essential to understand the scaling behavior and assessing the effect of the pixel resolution on the energy balance fluxes. Future research can follow the procedures presented in this study for different surfaces and conditions. Also, the uncertainty analysis of aggregated input forcing data set at coarser resolution can be used to study and better understand its influence on the final flux estimation on various scales/resolutions.

Acknowledgment

This study is based upon work that is supported by the National Institute of Food and Agriculture, U.S. Department of Agriculture, Hatch Project, under the Project Number NEB-21-155. This study was also supported by the grants from the Central Platte Natural Resources District (CPNRD) under the grant agreement 38484, Nebraska Environmental Trust (NET) under the project agreement #13-146, and Nebraska Department of Natural Resources (NEDNR) under the project agreement #477. The authors express their appreciation to USDA-AFRI, CPNRD, NET, and NEDNR. The data from this work are not publicly available; however, users can request data from Suat Irmak (e-mail: sirmak2@unl.edu) for scientific investigations. The mention of trade names or commercial products is for the information of the reader and does not constitute an endorsement or recommendation for use by the authors or their institution.

References

Allen, R. G., M. Tasumi, and R. Trezza (2007), Satellite-based energy balance for mapping evapotranspiration with internalized calibration (METRIC) model, *J. Irrig. Drain. Eng.*, *133*(4), 380–394.

Bastiaanssen, W., M. Menenti, R. Feddes, and A. Holtslag (1998), A remote sensing surface energy balance algorithm for land (SEBAL): 1. Formulation, *J. Hydrol.*, *212-213*, 198–212.

Bian, L. (1997), Multi-scale nature of spatial data in scaling up environmental models, in *Scale in Remote Sensing and GIS*, edited by D. A. Quattrochi and M. F. Goodchild, pp. 13–26, Lewis Publ., N. Y.

Bian, L., and R. Butler (1999), Comparing effects of aggregation methods on statistical and spatial properties of simulated spatial data, *Photogramm. Eng. Remote Sens.*, *65*, 73–84.

Brunsell, N. A. (2011), Characterizing the multi–scale spatial structure of remotely sensed evapotranspiration with information theory, *Biogeosciences*, *8*, 2269–2280.

Brunsell, N. A., and R. R. Gillies (2003), Scale issues in land–atmosphere interactions: Implications for remote sensing of the surface energy balance, *Agric. For. Meteorol.*, *117*(3), 203–221.

Brutsaert, W. (1982), *Evaporation Into the Atmosphere: Theory, History, and Applications*, Springer, Dordrecht, Netherlands.
Carmel, Y. (2004), Controlling data uncertainty via aggregation in remotely sensed data, *IEEE Geosci. Remote Sens. Lett.*, *1*(2), 39–41.
Chander, G., and B. Markham (2003), Revised Landsat-5 TM radiometric calibration procedures and post calibration dynamic ranges, *IEEE Trans. Geosci. Remote Sens.*, *41*(11), 2674–2677.
Chander, G., B. L. Markham, and J. A. Barsi (2007), Revised Landsat-5 thematic mapper radiometric calibration, *IEEE Trans. Geosci. Remote Sens. Lett.*, *4*(3), 490–494.
Choudhury, B., and J. Monteith (1988), A four-layer model for the heat budget of homogeneous land surfaces, *Q. J. R. Meteorol. Soc.*, *114*(480), 373–398.
Croley, I., T. E. C. He, and D. H. Lee (2005), Distributed-parameter large basin runoff model. II: Application, *J. Hydrol. Eng.*, *10*, 182–191.
Dodgson, N. A. (1997), Quadratic interpolation for image resampling, *IEEE Trans. Image Process.*, *6*(9), 1322–1326.
Ershadi, A., M. McCabe, J. Evans, and J. Walker (2013), Effects of spatial aggregation on the multi-scale estimation of evapotranspiration, *Remote Sens. Environ.*, *131*, 51–62.
Eugenio, F., and F. Marqués (2003), Automatic satellite image georeferencing using a contour-matching approach, *IEEE Trans. Geosci. Remote Sens.*, *41*(12), 2869–2880.
Famiglietti, J., and E. Wood (1994), Application of multiscale water and energy balance models on a tallgrass prairie, *Water Resour. Res.*, *30*(11), 3079–3093.
Fisher, J. B., K. P. Tu, and D. D. Baldocchi (2008), Global estimates of the land–atmosphere water flux based on monthly AVHRR and ISLSCP-II data, validated at 16 FLUXNET sites, *Remote Sens. Environ.*, *112*(3), 901–919.
Gibson, C. C., E. Ostrom, and T. Ahn (2000), The concept of scale and the human dimensions of global change: A survey, *Ecol. Econ.*, *32*(2), 217–239.
Giorgi, F. (1997), An approach for the representation of surface heterogeneity in land surface models. Part I: Theoretical framework, *Am. Meteorol. Soc.*, *125*(8), 1885–1899.
Guillevic, P. C., J. L. Privette, B. Coudert, M. A. Palecki, J. Demarty, C. Ottlé, and J. A. Augustine (2012), Land surface temperature product validation using NOAA's surface climate observation networks: Scaling methodology for the Visible Infrared Imager Radiometer Suite (VIIRS), *Remote Sens. Environ.*, *124*, 282–298.
Hong, S., J. M. Hendrickx, and B. Borchers (2009), Up-scaling of SEBAL derived evapotranspiration maps from Landsat (30 m) to MODIS (250 m) scale, *J. Hydrol.*, *370*(1), 122–138.
Irmak, S. (2010), Nebraska water and energy flux measurement, modeling, and research network (NEBFLUX), *Trans. ASABE*, *53*(4), 1097–1115.
Irmak, A., R. K. Singh, E. A. Walter-Shea, S. Verma and A. Suyker (2011), Comparison and analysis of empirical equations for soil heat flux for different cropping systems and irrigation methods, *Transactions of the ASABE*, *54*(1), 67–80.
Jia, L., G. Xi, S. Liu, C. Huang, Y. Yan, and G. Liu (2009), Regional estimation of daily to annual regional evapotranspiration with MODIS data in the Yellow River Delta wetland, *Hydrol. Earth Syst. Sci.*, *13*(10), 1775–1787.
Jiang, L., S. Islam, W. Guo, A. Singh Jutla, S. U. Senarath, B. H. Ramsay, and E. Eltahir (2009), A satellite-based daily actual evapotranspiration estimation algorithm over south Florida, *Global Planetary Change*, *67*(1), 62–77, doi:10.1016/j.gloplacha.2008.12.008.
Kustas, W. P., F. Li, T. J. Jackson, J. H. Prueger, J. I. MacPherson, and M. Wolde (2004), Effects of remote sensing pixel resolution on modeled energy flux variability of croplands in Iowa, *Remote Sens. Environ.*, *92*, 535–547.
Lam, N. S., and D. A. Quattrochi (1992), On the issues of scale, resolution, and fractal analysis in the mapping sciences, *Prof. Geogr.*, *44*(1), 88–98.
Liang, S. (2000), Numerical experiments on the spatial scaling of land surface albedo and leaf area index, *Remote Sens. Rev.*, *19*(1-4), 225–242.
Liang, S. (2005), *Quantitative Remote Sensing of Land Surfaces*, John Wiley, N. Y.
Long, D., V. P. Singh, and Z. Li (2011), How sensitive is SEBAL to changes in input variables, domain size and satellite sensor?, *J. Geophys. Res.*, *116*, D21107, doi:10.1029/2011JD016542.
Maayar, M. E., and J. M. Chen (2006), Spatial scaling of evapotranspiration as affected by heterogeneities in vegetation, topography, and soil texture, *Remote Sens. Environ.*, *102*, 33–51.
Ma, W., M. Hafeez, U. Rabbani, H. Ishikawa, and Y. Ma (2012), Retrieved actual ET using SEBS model from Landsat-5 TM data for irrigation area of Australia, *Atmos. Environ.*, *59*, 408–414.
Mason, P. (1988), The formation of areally-averaged roughness lengths, *Q. J. R. Meteorol. Soc.*, *114*(480), 399–420.
Massman, W. (1999), Molecular diffusivities of Hg vapor in air, O_2 and N_2 near STP and the kinematic viscosity and thermal diffusivity of air near STP, *Atmos. Environ.*, *33*(3), 453–457.
Menenti, M., and B. Choudhary (1993), Parameterization of land surface evapotranspiration using a location-dependent potential evapotranspiration and surface temperature range, in *Exchange Processes at the Land Surface for a Range of Space and Time Series*, edited by H. J. Bolle, R. A. Feddes, and J. D. Kalma, pp. 561–568, Publication 212, Int. Assoc. of Hydrol. Sci., Wallingford, U. K.
McCabe, M. F., and E. F. Wood (2006), Scale influences on the remote estimation of evapotranspiration using multiple satellite sensors, *Remote Sens. Environ.*, *105*(4), 271–285.
Mo, X., S. Liu, D. Chen, Z. Lin, R. Guo, and K. Wang (2009), Grid-size effects on estimation of evapotranspiration and gross primary production over a large Loess Plateau basin, China, *J. Hydrol. Sci.*, *54*(1), 160–173.
Monin, A. S., and A. M. Obukhov (1954), Basic laws of turbulent mixing in the atmosphere near the ground, *Trudy Geofiz. Inst. Akad. Nauk SSSR*, *24*(151), 163–187.
Moran, S., S. Humes, and P. J. Pinter Jr. (1997), The scaling characteristics of remotely-sensed variables for sparsely-vegetated heterogeneous landscapes, *J. Hydrol.*, *190*(3), 337–362.
Nellis, M. D., and J. M. Briggs (1989), The effect of spatial scale on Konza landscape classification using textural analysis, *Landscape Ecol.*, *2*(2), 93–100.
Paulson, C. A. (1970), The mathematical representation of wind speed and temperature profiles in the unstable atmospheric surface layer, *J. Appl. Meteorol.*, *9*(6), 857–861.
Raupach, M. R. (1992), Drag and drag partition on Rough Surfaces, *Boundary Layer Meteorol.*, *60*(4), 375–395.
Raupach, M. R. (1995), Vegetation atmosphere interaction and surface conductance at leaf, canopy and regional scales, *Agric. For. Meteorol.*, *73*(3-4), 151–179.
Roerink, G., Z. Su, and M. Menenti (2000), S-SEBI: A simple remote sensing algorithm to estimate the surface energy balance, *Phys. Chem. Earth*, *25*(2), 147–157.
Samani, Z., A. S. Bawazir, M. Bleiweiss, R. Skaggs, and V. D. Tran (2007), Estimating daily net radiation over vegetation canopy through remote sensing and climatic data, *J. Irrig. Drain. Eng.*, *133*(4), 291–297.

Schoorl, J., M. Sonneveld, and A. Veldkamp (2000), Three-dimensional landscape process modelling: The effect of DEM resolution, *Earth Surf. Processes Landforms*, *25*(9), 1025–1034.
Schuepp, P., M. Leclerc, J. MacPherson, and R. Desjardins (1990), Footprint prediction of scalar fluxes from analytical solutions of the diffusion equation, *Boundary Layer Meteorol.*, *50*(1-4), 355–373.
Seyfried, M., and B. Wilcox (1995), Scale and the nature of spatial variability: Field examples having implications for hydrologic modeling, *Water Resour. Res.*, *31*(1), 173–184.
Sharma, V., S. Irmak, A. Kilic, and D. Mutiibwa (2015), Application of remote sensing for quantification and mapping surface energy fluxes in south central Nebraska: Analyses with respect to field measurements, *Trans. ASABE*, *58*(5), 1265–1285, doi:10.13031/trans.58.11091.
Shu, Y., S. Stisen, K. H. Jensen, and I. Sandholt (2011), Estimation of regional evapotranspiration over the North China Plain using geostationary satellite data, *Int. J. Appl. Earth Obs. Geoinf.*, *13*(2), 192–206.
Singh, R. K., A. Irmak, S. Irmak, and D. L. Martin (2008), Application of SEBAL model for mapping evapotranspiration and estimating surface energy fluxes in south-central Nebraska, *J. Irrig. Drain. Eng.*, *134*(3), 273–285, doi:10.1061/(ASCE)0733-9437(2008)134:3(273).
Sobrino, J. A., J. C. Jiménez-Muñoz, and L. Paolini (2004), Land surface temperature retrieval from LANDSAT TM 5, *Remote Sens. Environ.*, *90*(4), 434–440.
Sridhar, V., R. L. Elliott, and F. Chen (2003), Scaling effects on modeled surface energy-balance components using the NOAH-OSU land surface model, *J. Hydrol.*, *280*(1), 105–123.
Su, H., M. McCabe, E. Wood, Z. Su, and J. Prueger (2005), Modeling evapotranspiration during SMACEX: Comparing two approaches for local-and regional-scale prediction, *J. Hydrol. Meteorol.*, *6*(6), 910–922.
Su, Z. (2002), The Surface Energy Balance System (SEBS) for estimation of turbulent heat fluxes, *Hydrol. Earth Syst. Sci. Discuss.*, *6*(1), 85–100.
Su, Z., H. Pelgrum, and M. Menenti (1999), Aggregation effects of surface heterogeneity in land surface processes, *Hydrol. Earth Syst. Sci.*, *3*(4), 549–563.
Vieux, B. E. (1993), DEM aggregation and smoothing effects on surface runoff modeling, *J. Comput. Civ. Eng.*, *7*(3), 310–338.
Vinukollu, R. K., E. F. Wood, C. R. Ferguson, and J. B. Fisher (2011), Global estimates of evapotranspiration for climate studies using multi-sensor remote sensing data: Evaluation of three process-based approaches, *Remote Sens. Environ.*, *115*(3), 801–823.
Wang, L., G. Parodi, and Z. Su (2008), SEBS module BEAM: A practical tool for surface energy balance estimates from remote sensing data, paper presented at The 2nd MERIS-(A) ATSR Workshop, edited, ESRIN, Frascati, Italy.
Wang, Z., B. Zhang, S. Zhang, X. Li, D. Liu, K. Song, J. Li, F. Li, and H. Duan (2006), Estimation of evaporative fraction from a combination of day and night land surface temperatures and NDVI: A new method to determine the Priestley–Taylor parameter, *Remote Sens. Environ.*, *102*, 293–305.
Webb, E. K. (1970), Profile relationships: The log-linear range, and extension to strong stability, *Q. J. R. Meteorol. Soc.*, *96*(407), 67–90.
Wieringa, J. (1986), Roughness-dependent geographical interpolation of surface wind speed averages, *Q. J. R. Meteorol. Soc.*, *112*(473), 867–889.
Zhang, W., and D. R. Montgomery (1994), Digital elevation model grid size, landscape representation, and hydrologic simulations, *Water Resour. Res.*, *30*(4), 1019–1028.